

Early formation of primitive achondrites in an outer region of the protoplanetary disc

N. Ma, W. Neumann, A. Néri, W.H. Schwarz, T. Ludwig,
M. Tieloff, H. Klahr, A. Bouvier

Supplementary Information

The Supplementary Information includes:

- Methods
- Supplementary Discussion
- Tables S-1 to S-8 (.xlsx file)
- Figures S-1 to S-13
- Supplementary Information References

Methods

Petrographic methods

Polished mounts and thin sections of Tafassasset, NWA 7317, NWA 11561, and NWA 12455 (donated from Ben Hoefnagels, Big Bang Meteorites, or purchased from Marcin Cimała, Polandmet Meteorites) were prepared and characterised first under optical microscopy to estimate weathering and shock level. Polished mounts were first carbon-coated to acquire multi-field BSE-EDS element maps (elements preselected to be Na, Mg, Al, Si, P, O, Fe, Ca, Ti, Cr, Ni, S, Cl) using a focused ion beam scanning electron microscopy (FEI Scios FIB-SEM) at Bayerisches Geoinstitut (BGI), Universität Bayreuth, with an electron beam tuned to 20 kV and 1.6 nA. Subsequent petrographic observations were carried out using a Zeiss Gemini 1530 scanning electron microscope (BGI) operated at 20 kV under BSE-EDS mode. Mineral compositions were measured using a JEOL JXA 8200 electron microprobe (BGI) equipped with five

spectrometers operated at 15 kV and 15 nA with ~1 µm focused electron beam (5 µm for merrillites) and counting time of 20 s on peak, 10 s on background (10 s on peak for Na, Cl and F, and 5 s on background to reduce the beam induced damage and loss of volatiles during analysis). The standards used and respective detection limits (D.L. for pure elements in ppm) are: Na and Si (albite, 249 ppm and 135 ppm), Ca (wollastonite or apatite, 129 ppm), K (orthoclase, 133 ppm), Mg (enstatite, 115 ppm), Fe (Fe metal, 218 ppm), Mn and Ti (MnTiO₃, 272 ppm and 175 ppm), Al (spinel, 140 ppm), Ni (Ni metal, 191 ppm), Cr (Cr metal, 274 ppm), S (pyrite, 258 ppm), P (apatite, 228 ppm), Cl (tugtupite, 127 ppm), F (fluorite, 478 ppm). The PRZ method was used for matrix correction.

Secondary ion mass spectrometry (SIMS) Pb–Pb merrillite dating

Polished mounts were cleaned with alcohol, dried, and coated with a 50 nm gold layer before SIMS analysis. High precision ²⁰⁷Pb–²⁰⁶Pb phosphate dating was performed using a Cameca IMS 1280-HR secondary ion mass spectrometer (SIMS) at the Heidelberg Ion Probe (HIP), Universität Heidelberg. A Duoplasmatron ion source was operated to generate a primary O⁻ ion beam with 23 kV impact energy, 20–40 nA beam current and beam size of 20–30 µm on the sample surface. Prior to each analysis, a two-minute pre-sputtering was applied to remove potential surface contamination. Positive secondary ions of ⁴⁰Ca₂³¹P¹⁶O₄⁺, ²⁰⁴Pb⁺, ²⁰⁶Pb⁺, ²⁰⁷Pb⁺, ²³⁸U⁺, ²³⁸U¹⁶O⁺ were extracted, mass filtered at a mass resolution (M/ΔM) of ~4000 before sequential detection in an ion-counting electron multiplier for 1s, 20s, 10s, 10s, 10s and 6s, respectively in single collection mode. Thirty cycles per analysis were typically applied for better statistics. ⁴⁰Ca₂³¹P¹⁶O₄⁺ was used for peak centring and ²³⁸U¹⁶O⁺ for calculating U and Pb secondary ion yields.

Raw data were reduced and calibrated against measurements of standard Madagascar apatite (485 Myr, Thomson *et al.*, 2012) using in-house-developed software (ZIPS version 3.1.1, by Christopher Coath). Common lead correction was made using the composition and model of Stacey and Kramers (1975) and primordial Pb isotopic composition reported for Canyon diablo troilite by Tatsumoto *et al.* (1973). In the absence of suitable merrillite standard, U and Pb secondary ion yields were not known precisely. Therefore, U/Pb systematics cannot be measured with satisfactory accuracy. But if the analysed points were used as hypothetical standard, all results plotted tightly into a concordant cluster, strongly suggesting that the observed discrepancy is caused by a matrix effect (*i.e.* using apatite as standards for merrillite sample).

Due to the extremely high radiogenic Pb isotopic ratios measured for merrillites in Tafassites (common lead $^{204}\text{Pb} < 0.1$ cps, and $^{204}\text{Pb}/^{206}\text{Pb}$ ratio on the order of 10^{-4} – 10^{-5}), the choice of the apatite standard (as comparably-aged apatite or merrillite standards are not available) as well as primordial Pb isotopic ratio did not affect the calculated Pb–Pb merrillite ages. The ^{207}Pb – ^{206}Pb ages of individual analyses (Table S-5) were calculated from the radiogenic $^{207}\text{Pb}^*/^{206}\text{Pb}^*$ ratio using the decay constant of Steiger and Jäger (1977), $^{238}\text{U}/^{235}\text{U} = 137.82 \pm 0.05$ (Hiess *et al.*, 2012), with individual age uncertainties of 0.8–2.4% ($\pm 2\sigma$, except for Tafassasset which was 2.2–4.4%, as a result of lower U concentrations and therefore less radiogenic compositions). In the end, the ^{207}Pb – ^{206}Pb merrillite age for each sample was reported as weighted mean with typical uncertainties of 4–16 Myr ($\pm 2\sigma$).

Closure temperatures and oxygen fugacity calculations

To add additional constraints to the formation condition of Tafassites, closure temperatures and oxygen fugacity conditions were calculated and results are presented in Table S-3. A closure temperature corresponds to the temperature at which a system gets “frozen”, alternatively it can be considered as the last temperature of equilibration between minerals. Such temperatures are to be used to estimate the oxygen fugacity conditions. Noteworthy, these calculations only give access to the cooling conditions.

To calculate closure temperatures, two mineral pairs were considered: (1) the olivine-chromite pair and (2) the two-pyroxene pair. The first mineral pair assumes equilibrium of the Fe^{2+} -Mg exchange reaction between olivine and spinel, following: $\text{Fe}_2\text{SiO}_4 + 2 \text{MgAl}_2\text{O}_4 = \text{Mg}_2\text{SiO}_4 + 2 \text{FeAl}_2\text{O}_4$. Equilibrium condition was calculated using the online MELTS olivine-spinel-orthopyroxene geothermometer-oxybarometer (Sack and Ghiorso, 1989; 1991, 1994a,b,c; Ghiorso and Sack, 1991, Kretz, 1982). Although contacting pairs are scarce across sample sections, mineral compositions are extremely homogeneous, thus input compositions were considered as the average obtained from EPMA measurements. The Fe^{3+} content of our Cr-spinel was recalculated using the SPINCALC spreadsheet from GabbroSoft (<https://www.gabbrosoft.org/spreadsheets/>); this calculator verifies that the spinel composition is feasible in terms of stoichiometry and, if not, balances the amount of iron between the 2+ and 3+ valence. The second mineral pair considers the solvus between clino- and orthopyroxene through the transfer of the enstatite component from one pyroxene to another. To this aim, an existing parametrisation of the solvus slope was used (Kretz, 1982); here also the averaged

mineral compositions were used as input. Values found in this study are slightly larger than existing literature data on Tafassasset (Gardner-Vandy *et al.*, 2012), of 30 K and 60 K for the olivine-chromite the two pyroxene mineral pairs respectively. One could argue that such differences may rise from the use of different thermodynamic models, a concern that is justified regarding the two-pyroxene thermometer but not the olivine-chromite one. Indeed, the Kretz two-pyroxene thermometer was used here (Kretz, 1982), while previous studies on Tafassasset used the one from Lindsley and Andersen (1983) and Andersen *et al.* (1993) implemented on QUILF. In their study, Lindsley and Andersen made a thorough comparison of the existing two-pyroxene thermometers in a variety of applications, both on natural and experimental samples, and found that Kretz' thermometer yields most similar temperatures. Compositional variations may also be responsible for such variations. In previous studies (Benedix *et al.*, 2005; Schrader *et al.*, 2017a), standard deviations on measured compositions were estimated to result in closure temperature uncertainties of ± 50 K and ± 100 K, respectively for the olivine-chromite and two-pyroxene pairs. The observed differences of closure temperatures are thus well within the uncertainty range.

Similarly to previous studies (Gardner-Vandy *et al.*, 2012; Schrader *et al.*, 2017a), the oxygen fugacity can be determined from the calculated closure temperatures and using the Quartz-Iron-Fayalite (QIFa) and Quartz-Iron-Ferrosilite (QIFs) equilibria:



The temperature dependence of the equilibrium constants of these reactions has been calculated in previous work (Gardner-Vandy *et al.*, 2012) and can be linked to the activity of the different species. Based on experimental efforts, it has been argued that the activity of silica can be set to 0.93 (Benedix *et al.*, 2005, Larimer, 1968); using slightly different values does not give drastically different results (Schrader *et al.*, 2017a). The activity of iron was calculated from the Fe-Ni composition of kamacite-taenite grains assuming an ideal solid solution. Finally, the activity coefficients of fayalite and ferrosilite were estimated from the measured compositions using the online MELTS Supplemental Calculator (Ghiorso and Sack, 1995). Thus, only the activity coefficient of O_2 , *i.e.* the oxygen fugacity, remains unknown and can be calculated. Results in log units are shown in Table S-3 and are compared to the Iron-Wüstite (IW) buffer (O'Neill and Pownceby, 1993).



For each sample, a calculated oxygen fugacity has deviations from the IW buffer (ΔIW) that is within 0.1 log unit identical when considering either the QIFa or QIFs equilibrium. This feature indicates no significant oxygen fugacity variation during cooling over this temperature interval. Besides, throughout the sample survey, the ΔIW values are extremely homogeneous, about -1.4 log units. A 0.5 log unit difference can be observed when comparing our ΔIW values to existing data on Tafassasset T7 (Gardner-Vandy *et al.*, 2012). Seemingly, authors used a different thermodynamic description of the IW buffer than that of O'Neill and Pownceby (1993). Indeed, using published closure temperature and phase compositions, we were unable to reproduce the ΔIW values, though we retrieved the exact same absolute oxygen fugacities. Instead, we obtained $\Delta IW = -1.3$ and $\Delta IW = -1.5$ for the QIFa and QIFs equilibria respectively, which are now identical to the ones determined for the Tafassasset and Tafassite polished sections studied here.

Thermal history modelling

Energy balance. 1D finite differences thermal evolution model for planetesimals heated mainly by ^{26}Al similar to Neumann *et al.* (2012, 2018) was adapted. This model calculates heating of small porous bodies, their thermal evolution, compaction of a mixture of dry and hydrated material from an initially unconsolidated state due to hot pressing, and metal-silicate differentiation by solving a number of equations that describe these processes. The model description presented in Fig. 3 is provided in the following. A non-stationary 1D heat conduction equation in spherical coordinates is discretised by the finite difference method along the spatial and temporal domain and solved for the temperature:

$$\rho c_p (1 + x_{ice} S_{ice} + x_{Fe} S_{Fe} + x_{Si} S_{Si}) \frac{\partial T}{\partial t} = \frac{1}{r^2} \frac{\partial}{\partial r} \left(k r^2 \frac{\partial T}{\partial r} \right) + Q(r, t) \quad \text{Eq. S-1}$$

with the bulk density ρ , the heat capacity c_p , the initial fractions x and Stefan numbers S for water ice, metal (Fe), and silicates (Si), the temperature T , the time t , the radius variable r , and the energy source density Q . The energy source for the temperature change is radioactive decay of typical short-lived radionuclides ^{26}Al and ^{60}Fe and long-lived ^{40}K , ^{232}Th , ^{235}U , and ^{238}U (Table S-8):

$$Q(r, t) = \rho \sum_i f_i Z_i \frac{E_i}{\tau_i} \exp\left(-\frac{t-t_0}{\tau_i}\right) \quad \text{Eq. S-2}$$



with the porosity-dependent bulk density ρ , the number of atoms of a stable isotope per kg of the primordial material f , the initial ratio of radioactive and stable isotope Z , the decay energy E , the mean life $\tau = \lambda/\log(2)$, the half-life λ , and the accretion time t_0 of the planetesimal. A homogeneous heat source distribution within the material is assumed, while the heat source density scales further with the porosity ϕ . The porosity is initially constant throughout the interior but develops heterogeneously with depth during the thermal evolution under the action of temperature and pressure. The temperature calculation starts from an initial value of $T_S = 120$ K with a surface temperature T_S . In our modelling, we used the canonical ratio of $^{26}\text{Al}/^{27}\text{Al} = 5.25 \times 10^{-5}$ (Table S-8). If we assumed a much lower initial $^{26}\text{Al}/^{27}\text{Al}$ of 1×10^{-5} and 1.5×10^{-5} (4 to 5 times lower than the canonical ratio) that have been proposed for CR chondrites and inner NC solar system objects, respectively (Van Kooten *et al.*, 2016; Bollard *et al.*, 2019), the predicted PB accretion ages would be significantly older and in fact even older than CAIs. We find ~ 0.5 Myr before CAI formation for Tafassite PB, and > 1.0 Myr for magmatic NC irons. Even if this was the case, this will not affect our conclusion that Tafassites have to form substantially earlier than CR chondrites and as such they cannot originate from a common parent body.

Composition and material properties. Based on compositional similarities of Tafassites with ordinary chondrites and acapulcoites, we assume properties similar to an H chondrite (Neumann *et al.*, 2012) approximated roughly with a grain density of $\rho_g = 3690$ kg m⁻³, a metal (free Fe, Ni and sulfides) mass fraction of $x_{\text{Fe}} = 0.22$ (or a volume fraction of $v_{\text{Fe}} = 0.12$) with a metal density of $\rho_{\text{Fe}} = 6811$ kg m⁻³, and a silicate mass fraction of $x_{\text{Si}} = 0.78$ (or a volume fraction of $v_{\text{Si}} = 0.88$) with a silicate density of $\rho_{\text{Si}} = 3270$ kg m⁻³. This composition is reasonably representative in terms of the thermal evolution and compaction behaviour. The local bulk density ρ is derived from the grain density ρ_g by scaling it with the local volume filling factor $(1-\phi)$: $\rho = (1-\phi)\rho_g$. The equations for the heat capacity c_p and the thermal conductivity k are averages of the metal and silicate contributions, where k is porosity-dependent (Neumann *et al.*, 2012). We assumed an initial ice mass fraction of $x_{\text{ice}} = 0.04$ (similar to carbonaceous chondrites, Alexander *et al.*, 2013) and include the consumption of the latent heat during the melting of a potentially initially present water ice.

Porosity. The evolution of the bulk pore space volume fraction, *i.e.* porosity ϕ is calculated by considering creep of dry olivine as an approximation of the bulk material. It is described by a non-stationary differential equation for a strain rate-stress relation. The strain rate is calculated from a diffusion creep equation for the deformation of dry olivine derived by Schwenn and Goetze (1978):



$$\dot{\epsilon} = \frac{\partial \log(1-\phi)}{\partial t} = A\sigma^n b^{-m} \exp\left(-\frac{E}{RT}\right) \quad \text{Eq. S-3}$$

Here, the pre-factor is $A = 1.26 \cdot 10^{-18}$, the stress σ is in Pa, the stress exponent $n = 1.5$, the grain size $b = 10^{-5}$ m, the grain size exponent $m = -1.4$, activation energy $E = 356$ kJ mol⁻¹, the gas constant $R = 0.008314$ kJ mol⁻¹ K⁻¹ and the temperature T in K. An initial porosity of $\phi_0 = 0.5$ is a typical value based on the porosities of the random loose and random close packings. The effective stress σ is calculated for the simple cubic packing of equally sized spheres that has a porosity of ~50 % (Henke *et al.*, 2012; Neumann *et al.*, 2014).

Melting and differentiation. The melting of water ice is considered in a temperature interval of two degrees between $T = 272$ K and $T = 274$ K in order to avoid numerical issues with too sharp a phase transition at 273 K. For simplification, we considered a linear metal melt production between the metal solidus and liquidus temperatures of 1213 K and 1700 K, respectively, and a linear silicate melt production between the silicate solidus and liquidus of 1325 K and 1700 K, respectively, such that a silicate melting degree of 20 % is produced at $T = 1400$ K (Breton *et al.*, 2015). In all three cases, the latent heats of ice, metal, and silicates of $3.34 \cdot 10^5$ J kg⁻¹K⁻¹, $2.7 \cdot 10^5$ J kg⁻¹K⁻¹, and $4 \cdot 10^5$ J kg⁻¹K⁻¹, respectively, contribute to the energy balance via the modification of the heat capacity with a Stefan number weighted with the respective mass fractions. The separation of metal from silicates are calculated as Neumann *et al.*, (2012, 2018). In addition, cooling by liquid-state convection at temperatures above 1650 K (*i.e.* in a magma ocean) is calculated by parametrising the thermal conductivity at the respective depths.

Radius and resolution. The radius $R(t)$ of the object considered changes with the bulk porosity $\phi_{\text{bulk}}(t)$ at the time t , obtained by integrating the local porosity over the radius r , according to:

$$R(t) = (1 - \phi_{\text{bulk}})^{-1/3} R \quad \text{Eq. S-4}$$

where R is the reference radius, *i.e.* the radius at zero porosity. The reference radius is used for the analysis of the results since it is representative for sets of bodies with equal mass and grain density, but different porosity. All equations involved are solved on the spatial radius domain ranging from the centre of the planetesimal up to its surface. The spatial grid is transformed from $0 \leq r \leq R$, with the distance from the centre r in m, to $0 \leq \eta \leq 1$ using the transformation $\eta = r/R(t)$. The time and space derivatives are transformed as well and the transformed expressions are applied to all

equations involved, such that features like Lagrangian transport of porosity and of other quantities are accounted for. While the positions of the grid points between 0 and 1 are fixed, the variable values at the grid points are updated at every timestep according to the above transformations. The number of grid points is adapted such that the resolution in the outer 10 km of the planetesimal is ~10 m for the fit procedure. Non-stationary equations are discretised also with respect to the time variable t and solved using implicit finite difference method.

Fitting Procedure. We use an approach utilised in several H and L chondrite parent body studies (Gail and Trieloff, 2019; Henke *et al.*, 2012) and a study of the acapulcoite-lodranite parent body (Neumann *et al.*, 2018) to fit the thermo-chronological data with a least square procedure, *i.e.* by calculating the root mean square offset (RMS). The goal of the fitting procedure is to find model parameters that result in a thermal evolution model for the parent body which reproduces the thermo-chronological data as close as possible. For this, a thermal evolution model is calculated for a given set of model parameters. Then, for each of the meteorites a burial depth d is assumed. The quality can be determined by calculating the distances of the temperature curves $T(t,d)$ to each of the data points. We denote the measured closure time and the closure temperature of one of the radioactive decay systems (enumerated with index i) as t_i^c and T_i^c , respectively. The temperature curve $T(t,d)$ has in general a shape with an increase during the first million years until the maximum temperature T_{max} is achieved at a certain time t_{max} , followed by a cooling phase. To determine the quality of the model, we distinguish between two cases for each data point:

1. If the maximum temperature T_{max} is higher than the corresponding closure temperature T_i^c , the summed distance of the temperature curve to the data points is defined by:

$$\delta(d) = \sum_i \frac{(t_i^c - t(T_i^c))^2}{\sigma_{t,i}^2} + \frac{(T_i^c - T(t_i^c, d))^2}{\sigma_{T,i}^2} \quad \text{Eq. S-5}$$

where $t(T_i^c)$ is the time at which the temperature curve passed the closure temperature T_i^c on its descending branch, $T(t_i^c, d)$ is the temperature achieved at the depth d at the closure time t_i^c , and $\sigma_{t,i}$ and $\sigma_{T,i}$ are the errors of the determination of the closure temperatures and cooling ages, respectively.

2. If the maximum temperature T_{max} does not surpass the closure temperature T_i^c throughout the model time, the distance is determined by:

$$\delta^2(d) = \sum_i \frac{(t_i^c - t_{max})^2}{\sigma_{t,i}^2} + \frac{(T_i^c - T_{max})^2}{\sigma_{T,i}^2} \quad \text{Eq. S-6}$$

Our data set for Tafassites comprises four meteorites – Tafassasset, NWA 11561, NWA 7317, and NWA 12455. For Tafassasset, we consider three data points, while the other three have one data point each. Thus, for Tafassasset, $\delta^2(d)$ has three summands corresponding to the respective radioactive decay systems, while for each NWA meteorite $\delta^2(d)$ has one summand. Furthermore, typical metamorphic temperatures for highly equilibrated chondrites of 1297 K to 1455 K (Dodd, 1969) are used to penalise the depths at which the maximum temperature does not agree with the metamorphic temperatures for the NWA meteorites:

$$P_{NWA} = \max\{T_{max} - 1455, 0\} - \min\{T_{max} - 1297, 0\} \quad \text{Eq. S-7}$$

by adding the penalty function to $\delta^2(d)$ in Eq. S-5 and S-6. Similarly, the depths at which the maximum temperature does not agree with the maximum temperature range of 1357 K to 1457 K for Tafassasset (Breton *et al.*, 2015), a penalty function:

$$P_{Tafa} = \max\{T_{max} - 1457, 0\} - \min\{T_{max} - 1357, 0\} \quad \text{Eq. S-8}$$

is added to $\delta^2(d)$ in Eq. S-5 and S-6.

With $\delta_j^2 := \min_d \delta(d)$, where j enumerates the different meteorites, we define the normalised quality function:

$$\chi_n = \left[\frac{1}{n} \sum_j \delta_j^2 \right]^{1/2} \quad \text{Eq. S-9}$$

by which we judge how good a given model fits our data set (here, n denotes the total number of the data points, $n = 6$). The penalty functions ensure that temperature curves with unrealistically high maximum temperatures that contradict the maximum temperature ranges for the meteorites but still would fit the data well on their descending branches are excluded. The values of the penalty function are zero within the allowed temperature ranges and adds a rapidly growing penalty the more the maximum T_{max} of a temperature curve deviates from this range. The fit procedure can result in

different burial depths for every meteorite considered. However, best fits for several NWA meteorites or for some NWA meteorites and Tafassasset can occur at the same depth.

Supplementary Discussion

Classification criteria of Tafassite meteorites

A minimum of 5 ungrouped and unpaired (not found together) meteorites are required by the Nomenclature Committee of the Meteoritical Society to form a new official group of meteorites based on similar whole-rock chemical and O-isotopic characteristics (Weisberg *et al.*, 2006). In cases of fewer than five meteorites, the term grouplet is used instead. In this study, 13 Tafassite meteorites (Table S-1) were classified as a new group of carbonaceous primitive achondrites (subdivided into petrological type 6 chondrites as T6, type 7 primitive achondrites as T7 and type 7 primitive achondrites with significant melt depletion as T7 depleted) according to the criteria listed below:

1. Highly equilibrated meteorites with prograding texture ranging from poikiloblastic with relict chondrules in T6 chondrites, poikilitic in T7 primitive achondrites with interstitial plagioclase and inverted pigeonite exsolution to protogranular in T7 primitive achondrites with melt depletion (Figs. S-1 and S-6 to S-11) and homogeneous mineral compositions (except for Plg when modified by partial melting, Table S-2). Despite extensive recrystallisation, heterogeneous mineralogical domains (vein/clastic in shape) are common at mm-to-cm scale (*e.g.*, NWA 11561 T7, Fig. S-10) with Plg- and Cpx-rich regions (predominant lithology) *vs.* opaque (particularly troilite-rich) and Mer-rich, Plg-poor clasts/veins, presumably reflecting incomplete textural homogenisation from a heterogeneous protolith (*e.g.*, monomict breccia). Due to high degrees of equilibration and common partial melting overprints, the abundance of refractory inclusions and matrix/chondrule ratio are difficult to reconstruct but observations made in NWA 7317 T6 suggest that Tafassites likely recrystallised from a relatively chondrule-poor protolith (Fig. S-8). The presence of relict chondrules on the other hand suggest that Tafassites accreted from chondritic materials. Thermodynamic calculations suggest Tafassites were equilibrated at 1117–1236 K (Ol-Chr), 1334–1413 K (two Px) and moderately oxidised oxygen fugacity (fO_2) of $\Delta IW -1.4 + 0.1$ (Fig. S-5 and Table S-3) consistent with observed interstitial plagioclase (indicative of

silicate partial melting $T > 1313$ K) and inverted pigeonite exsolution lamellae ($T > 1353$ K, Fig. S-6) in T7 primitive achondrites.

2. Tafassites comprise abundant Fe-rich olivine (Fa_{27-38} , Fe/Mn atomic ratios ranging 60–94, 40–80 vol. %), orthopyroxene (Fs_{23-31} , Fe/Mn 38–67), clinopyroxene (as exsolution lamellae in T7 primitive achondrites, two pyroxenes constitute 10–40 vol. %), intermediate plagioclase ($\text{An}_{28-56}\text{Ab}_{43-68}\text{Or}_{1-5}$, <1 to >10 vol. %, reflecting different degrees of melt loss) in coexistence of abundant Fe-Ni metal ($\sim\text{Fe}_{0.9}\text{Ni}_{0.1}$), troilite, Al-rich chromite ($\sim\text{Mg}_{0.2}\text{Fe}_{0.8}\text{Al}_{0.4}\text{Cr}_{1.5}\text{Ti}_{0.1}\text{O}_4$, 7–23 vol. % for all opaques) and trace merrillite ($\text{Na}_2\text{O} = 2.2$ wt. %, $\text{MgO} = 3.5$ wt. %, up to ~ 1 vol. %, Fig. S-7, Table S-1; and REE, Pb, Th, and U elemental concentrations in Table S-7).

3. At least most Tafassites experienced partial melting and are thus variably depleted in incompatible elements. Bulk chemical composition (Gardner-Vandy *et al.*, 2012; Göpel *et al.*, 2015) ranges from nearly chondritic to depleted in refractory lithophile and siderophile elements but enriched in Fe, Ni, Co relative to CI chondrites likely reflecting variable mineral abundances and/or melt extraction. Future bulk chemical analyses on T6 chondrites (*e.g.*, NWA 7317) might help to constrain if they still preserve chondritic element abundances.

4. Triple oxygen isotopic ratios fall on a mass-dependent fractionation line (slope ~ 0.51) below the terrestrial fractionation line (TFL), with a well-constrained $\Delta^{17}\text{O}$ anomaly of -1.67 ± 0.14 ‰ (Fig. 1 and Table S-4).

5. All 13 Tafassite samples known so far are of low weathering (W0–2), shock levels (S1–2) and found exclusively in the Sahara Desert. Complete pairing of specimens from each metamorphic group is excluded based on the described mineralogy, textures and mineral compositions summarised in Table S-1.

6. Available thermochronological data and thermal history modelling suggest the Tafassite parent body accreted early at $1.1^{+0.3}_{-0.4}$ Myr into a radius > 50 km before experiencing extreme thermal annealing ($T_{\text{peak}} > 1400$ K) and rapid cooling, *i.e.* 2.9 ± 0.9 Myr from ^{182}Hf – ^{182}W systematics with $T_c = 1200 \pm 50$ K (Breton *et al.*, 2015), 4.9 ± 0.3 Myr from ^{53}Mn –

^{53}Cr systematics with $T_c = 950 \pm 100$ K (Ito and Ganguly, 2006; Göpel *et al.*, 2015), and 9 ± 5 Myr from Pb–Pb phosphate ages (identical within uncertainty among the four Tafassites analysed in this study) with $T_c = 720 \pm 50$ K (Fig. 3) (all ages after CAI formation).

We used the published thermochronological data on Tafassasset (Breton *et al.*, 2015; Göpel *et al.*, 2015) and NWA 011, NWA 6704 grouplets CR chondrules, acapulcoites, basaltic achondrites and ordinary chondrite chondrules and phosphate ages (Göpel *et al.*, 1994; Schulz *et al.*, 2010; Bouvier *et al.*, 2011; Sugiura and Fujiya, 2014; Schrader *et al.*, 2017b; Pape *et al.*, 2019; Sanborn *et al.*, 2019) to compare different parent body evolution scenarios (Fig. 2). As short-lived radionuclide ages were reported using different anchors between studies and absolute U-corrected Pb–Pb ages have been also revised, we used the corresponding short-lived radiogenic systems and U-corrected Pb–Pb ages of D’Orbigny angrite corresponding to an absolute CAI age of ~ 4568 Ma when comparing Pb–Pb, Hf–W and Mn–Cr systematics of angrites, Tafassites, NWA 011 and NWA 6704 grouplets.

7. Carbonaceous-like nucleosynthetic anomalies (Burkhardt *et al.*, 2011; Fischer-Gödde *et al.*, 2015; Amelin *et al.*, 2019; Burkhardt *et al.*, 2019) *i.e.* $\epsilon^{50}\text{Ti} = 1.91\text{--}2.90$, $\epsilon^{54}\text{Cr} = 1.31\text{--}1.50$, $\epsilon^{94}\text{Mo} = 1.54 \pm 0.40$ and $\epsilon^{100}\text{Ru}_{\text{metal}} = -1.15 \pm 0.04$) of Tafassites which in addition to their sub TFL oxygen isotope compositions indicate that they accreted from C-like reservoir in the outer protoplanetary disc (Fig.S-13 and Tables S-4 and S-6).

Comparison of Tafassites with CR chondrites and other primitive achondrites

Tafassasset was previously classified from an equilibrated CR to ungrouped primitive achondrite (Bourot-Denise, 2002; Russel *et al.*, 2002; Gardner-Vandy *et al.*, 2012). The link to CR chondrites was based on (1) oxygen isotope similarity, (2) relict chondrules in Tafassasset claimed to be similar in morphology to chondrules in Renazzo CR2 and later (3) similar ^{54}Cr nucleosynthetic anomalies (Sanborn *et al.*, 2019). Therefore, Tafassasset and associated meteorites have been sometimes classified as equilibrated CR6/7 or CR-an (Burkhardt *et al.*, 2011; Irving *et al.*, 2014; Sanborn *et al.*, 2019; Agee *et al.*, 2020).

However, the higher bulk Fe contents in Tafassites (23–40 wt. %, vs. <28 wt. % for CR chondrites; Gardner-Vandy *et al.*, 2012), subchondritic Fe/Mn ratio in olivine and pyroxenes (Fig. S-3), the mass-dependent fractionation line with a slope of ~0.51 defined by Tafassites (*i.e.* uniform $\Delta^{17}\text{O}$ anomaly of -1.67 ± 0.14 ‰) vs. mass-independent mixing line in CR chondrites with a slope of ~0.71, Fig. 1) and distinctively earlier parent body formation (~1.1 Myr vs >4.0 Myr for CR parent body) all conclusively excluded a common parent body hypothesis. Instead, their mineralogy (*i.e.* enrichment Fe-Ni metals relative to other chondrite groups), overlapping O and mass-independent Cr and Ti isotopic signatures with CR, CH, and CB meteorites, would rather suggest a possibly long-lived common reservoir for metal-rich carbonaceous chondrites and achondrites.

Despite their apparent primitive achondrite-like texture and thermal history, distinctively higher bulk rock Fe contents, as manifested by high FeO contents in silicates coexisting with abundant opaques (Fe-Ni metal and sulfide), and the homogenised $\Delta^{17}\text{O}$ isotopic compositions distinguish Tafassites from any known groups of primitive achondrites (*i.e.* acapulcoite-lodranite, winonaite and brachinite groups; Fig. 1 and Fig. S-4), suggesting that Tafassites should instead constitute a new group of primitive achondrites.

Comparison with NWA 011 and NWA 6704 grouplets

NWA 011 grouplet meteorites. *i.e.* NWA 011, NWA 2400, NWA 2976, NWA 4901, NWA 4587, NWA 5644, NWA 7129, NWA 8545, and NWA 13274 (Yamaguchi *et al.*, 2002; Floss *et al.*, 2005; Russel *et al.*, 2005; Connolly *et al.*, 2007a, 2007b; Weisberg *et al.*, 2010; Garvie, 2012; Ruzicka *et al.*, 2013, 2014, 2015; Gattacceca *et al.*, 2020) are unbrecciated and ungrouped basaltic achondrites (Table S-1). Though broadly similar in mineralogy to eucrites, their higher Fe/Mn ratio in pyroxenes (Fig. S-3) and distinct oxygen isotopic composition ($\Delta^{17}\text{O} = -1.43$ to -1.86 ‰, Fig. 1) clearly suggest that they derive from a separate parent body other than asteroid 4 Vesta (Yamaguchi *et al.*, 2002; Floss *et al.*, 2005). While a possible linkage with CR/Tafassites-like meteorites has been suggested (Floss *et al.*, 2005; Irving *et al.*, 2014; Agee *et al.*, 2020) based on both FeO-rich mineral compositions and similar oxygen isotopic ratio, a common parent body source appears to be highly improbable for the following reasons: (1) FeO contents of olivine (up to Fa₈₅) and pyroxene (up to Fs₆₅) in NWA 011 grouplets are much higher than that of Tafassites (Fig. S-2); (2) higher

Fe/Mn ratio in pyroxene (Fig. S-3); (3) very Ca-rich plagioclase composition ($\sim\text{An}_{85}\text{Ab}_{15}\text{Or}_{<1}$ vs. $\sim\text{An}_{45}\text{Ab}_{54}\text{Or}_1$ in Tafassites). These suggest NWA 011-like incipient melts cannot be derived from partial melting and/or fractional crystallisation processes of a Tafassite/CR-like protolith. Rather, the differentiated lithology (*i.e.* basaltic achondrite ungrouped), ancient crystallisation ages (Fig. 1, Bogdanovski and Lugmair, 2004; Sugiura and Yamaguchi, 2007; Bouvier *et al.*, 2011), similar sub-TFL oxygen isotopic ratios (Yamaguchi *et al.*, 2002; Floss *et al.*, 2005), C-like Cr and Ti isotopes features (Bogdanovski and Lugmair, 2004; Trinquier *et al.*, 2009; Sanborn *et al.*, 2019) indicate NWA 011 grouplet meteorites likely represent another example of an early accreted differentiated parent body in the outer protoplanetary disc.

NWA 6704 grouplet meteorites. *i.e.* NWA 6704, NWA 6693, NWA 10132, and NWA 6926, Table S-1) are ungrouped differentiated pyroxenitic achondrites, likely of cumulative origin (Warren *et al.*, 2013; Koefoed, 2017; Amelin *et al.*, 2019; Hibiya *et al.*, 2019; Sanborn *et al.*, 2019). They are composed of predominant pyroxene ($\sim\text{Wo}_3\text{En}_{57}\text{Fs}_{40}$, ~ 70 vol. %), olivine ($\sim\text{Fa}_{52}$, 10–15 vol. %), Na-rich feldspar ($\text{Ab}_{>90}$, 10–15 vol. %) plus trace Ni-rich metal (awaruite), sulfide, chromite and merrillite. Also sometimes argued to be associated with CR/Tafassasset-like meteorites (Irving *et al.*, 2014; Agee *et al.*, 2020), the differentiated pyroxenitic lithology, higher FeO contents in silicates and higher oxygen fugacity ($\Delta\text{IW} +0.7$ (Warren *et al.*, 2013) vs. $\Delta\text{IW} -1.4$ in Tafassites, Table S-3), incompatible oxygen isotopic ratios ($\Delta^{17}\text{O} = -1.06 \pm 0.06$ ‰, Warren *et al.*, 2013; Hibiya *et al.*, 2019) but C-like nucleosynthetic anomalies (Fig. S-13) imply that NWA 6704 grouplet probably also originated from another early accreted and subsequently differentiated carbonaceous meteorite parent body accreted in the outer protoplanetary disc.

Supplementary Tables

Tables S-1 to S-8 are available for download (Excel) from the online version of this article at <https://doi.org/10.7185/geochemlet.2234>

Table S-1 List and petrological characteristics of Tafassite meteorites. Comparison with NWA 011 and NWA 6704 grouplets.

Table S-2 Chemical compositions of minerals in Tafassites measured by electron microprobe.

Table S-3 Thermodynamic calculation of equilibration temperature and oxygen fugacity of Tafassites.

Table S-4 Compilation of published oxygen isotopic data for Tafassites, NWA 011 and NWA 6704 grouplet meteorites.

Table S-5 Pb–Pb merrillite ages of Tafassites obtained by SIMS analysis.

Table S-6 Compilation of published nucleosynthetic anomaly data for Tafassites, NWA 011 and NWA 6704 grouplet meteorites.

Table S-7 Rare earth element, U, Th, and Pb concentration of merrillites in Tafassites measured by LA-ICP-MS.

Table S-8 Parameters used for the calculation of radiogenic energy.



Supplementary Figures

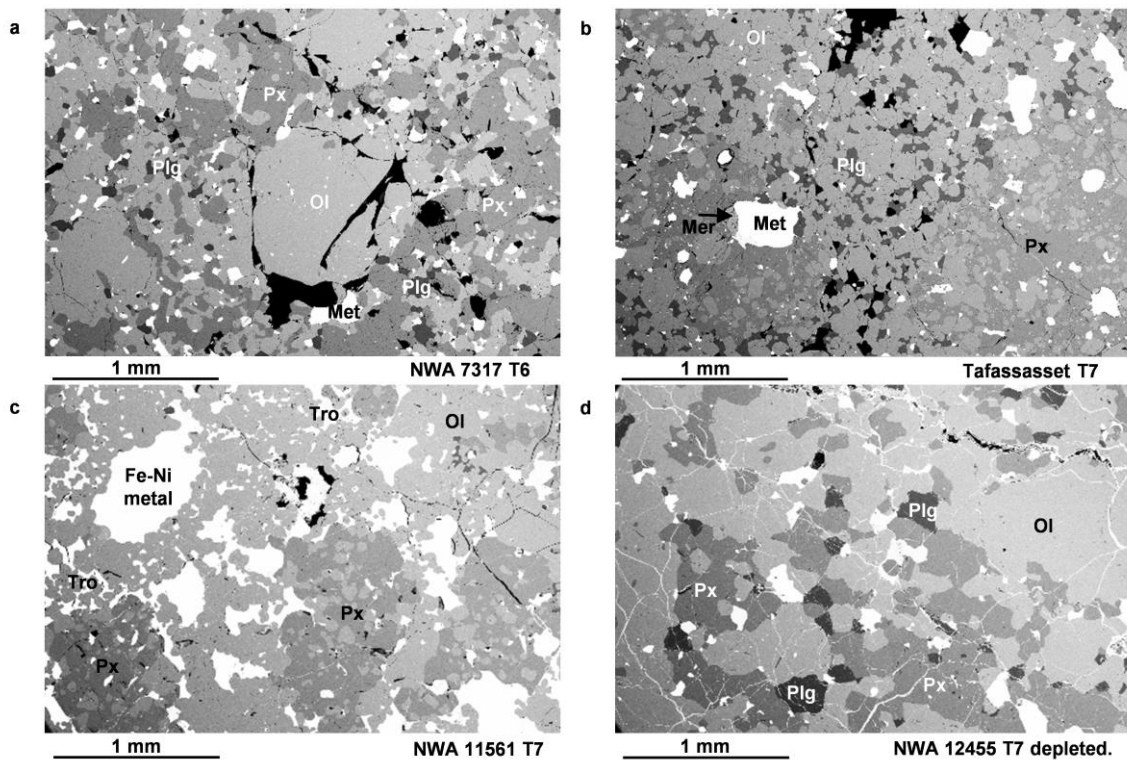


Figure S-1 Prograding textural variation of Tafassite meteorites. **(a)** NWA 7317 T6 chondrite with poikiloblastic texture, subsolidus heated at $T_{\text{peak}} < 1313$ K). **(b)** Tafassasset T7 primitive achondrite with poikilitic pyroxene (inverted pigeonite exsolution, interstitial plagioclase, supersolidus $T_{\text{peak}} > 1353$ K). **(c)** NWA 11561 T7 with poikilitic texture appears to be heterogeneous on the cm-scale section containing plagioclase (Plg)-poor, troilite (Tro), and merrillite (Mer)-rich domains with irregular boundaries (see also Fig. S-10). Similar features were also reported for Tafassasset. **(d)** NWA 12455 T7 dep. with protogranular texture (chondritic texture completely erased). The more equilibrated texture and depletion in incompatible components (*e.g.*, Plg, Px and Mer) suggest partial melt extraction.

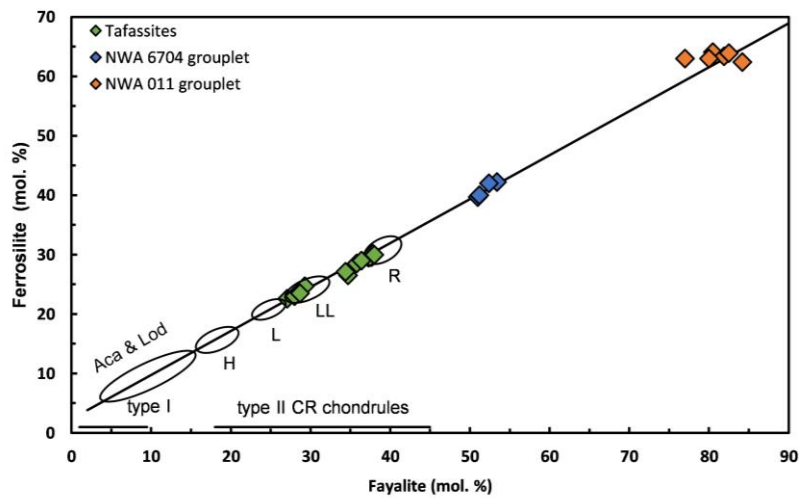


Figure S-2 FeO contents of olivine (fayalite end-member) and orthopyroxene (ferrosilite end-member) in Tafassites compared with CR chondrules NWA 011 and NWA 6704 grouplet meteorites (Tables S-1 and S-3).

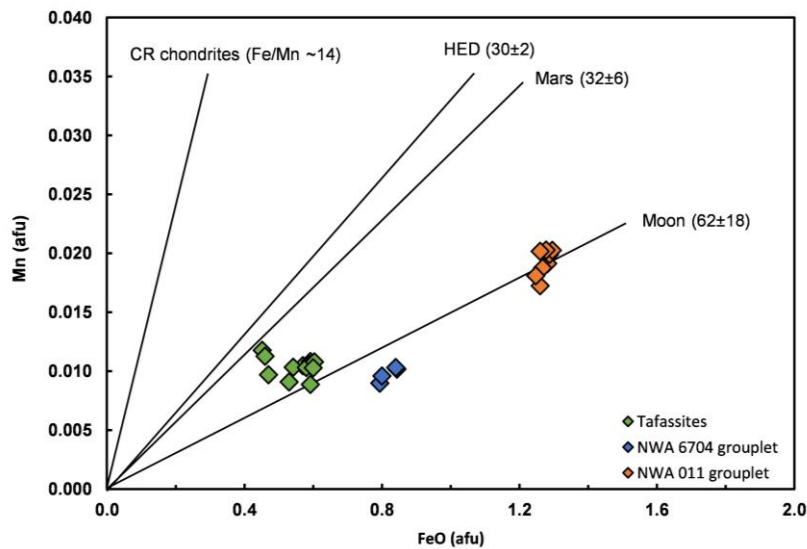


Figure S-3 Average Fe/Mn atomic ratios of pyroxenes in Tafassites, compared with bulk CR chondrites, NWA 6704 and NWA 011 grouplet meteorites (Table S-1, Fe/Mn trends from Papike *et al.* (2003) with average Fe/Mn atomic ratios shown in bracket with 1 σ , afu, atom per formula unit).

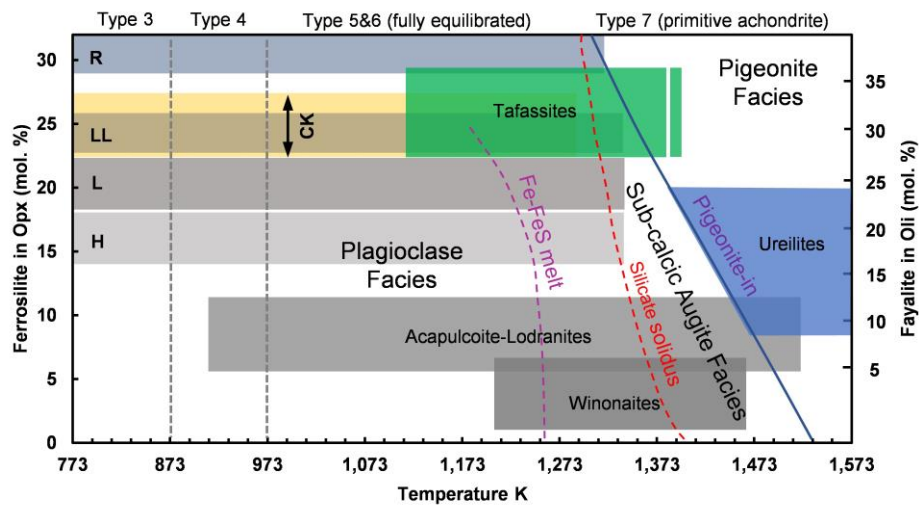


Figure S-4 Metamorphic facies diagram for equilibrated achondrite meteorites. Tafassites are highly equilibrated primitive achondrite meteorites that transect the chondrite-achondrite boundary (silicate solidus at ~1313 K) and distinguish themselves from the acapulcoites-lodranites and winonaites for much higher FeO contents in orthopyroxene and olivine, and from the brachinites for the presence of abundant Fe-Ni metal (after Tomkins *et al.*, 2020).

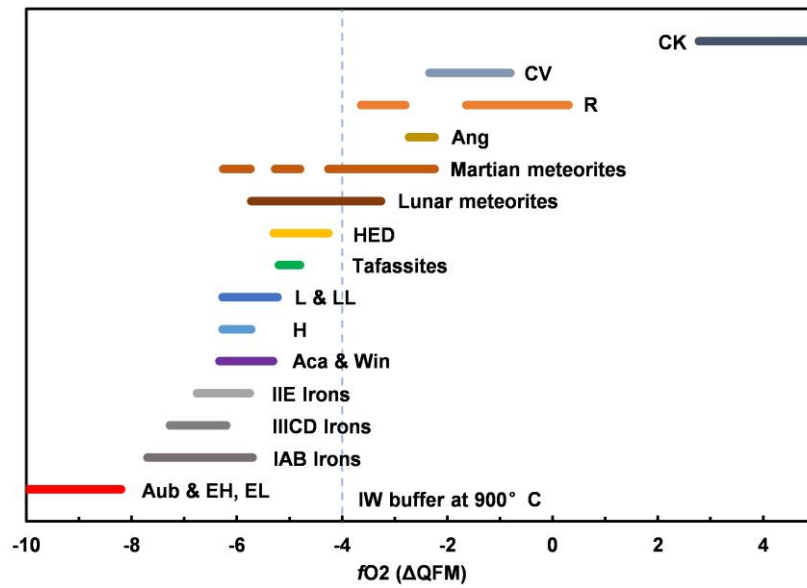


Figure S-5 Oxygen fugacity variation among meteorite groups relative to the fayalite-magnetite-quartz buffer (FMQ). The data for Tafassites are obtained from this study and reference data for other meteorite groups from Righter *et al.* (2006) and Righter and Neff (2007).

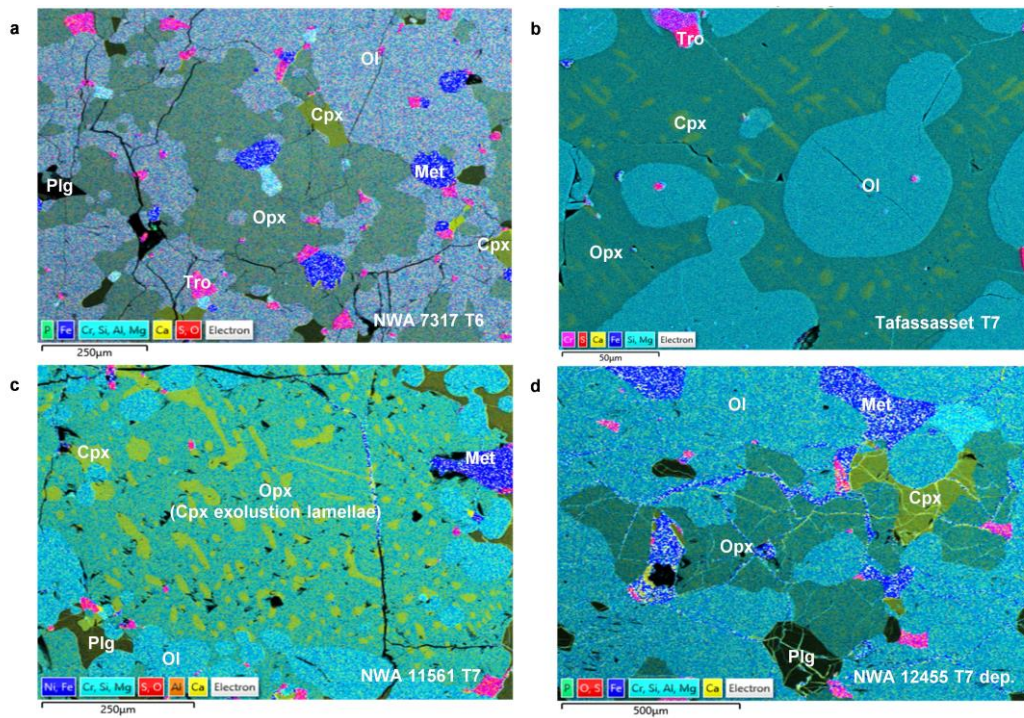


Figure S-6 The relationship of two pyroxenes in Tafassite meteorites shown by EDS element maps. **(a)** and **(d)**, Cpx and Opx exist as separate patches. Combining with other petrological evidence, NWA 7317 was probably equilibrated at just below subsolidus temperature ($T_{\text{peak}} < 1313$ K) while NWA 12455 was likely supersolidus heated, experienced partial melt loss and subsolidus re-equilibration. **(b)** and **(c)**, large patches of poikilitic pyroxenes occur as dominant Opx plus Cpx exsolution lamellae, a feature known as the inverted pigeonite exsolution ($T_{\text{peak}} > 1353$ K).

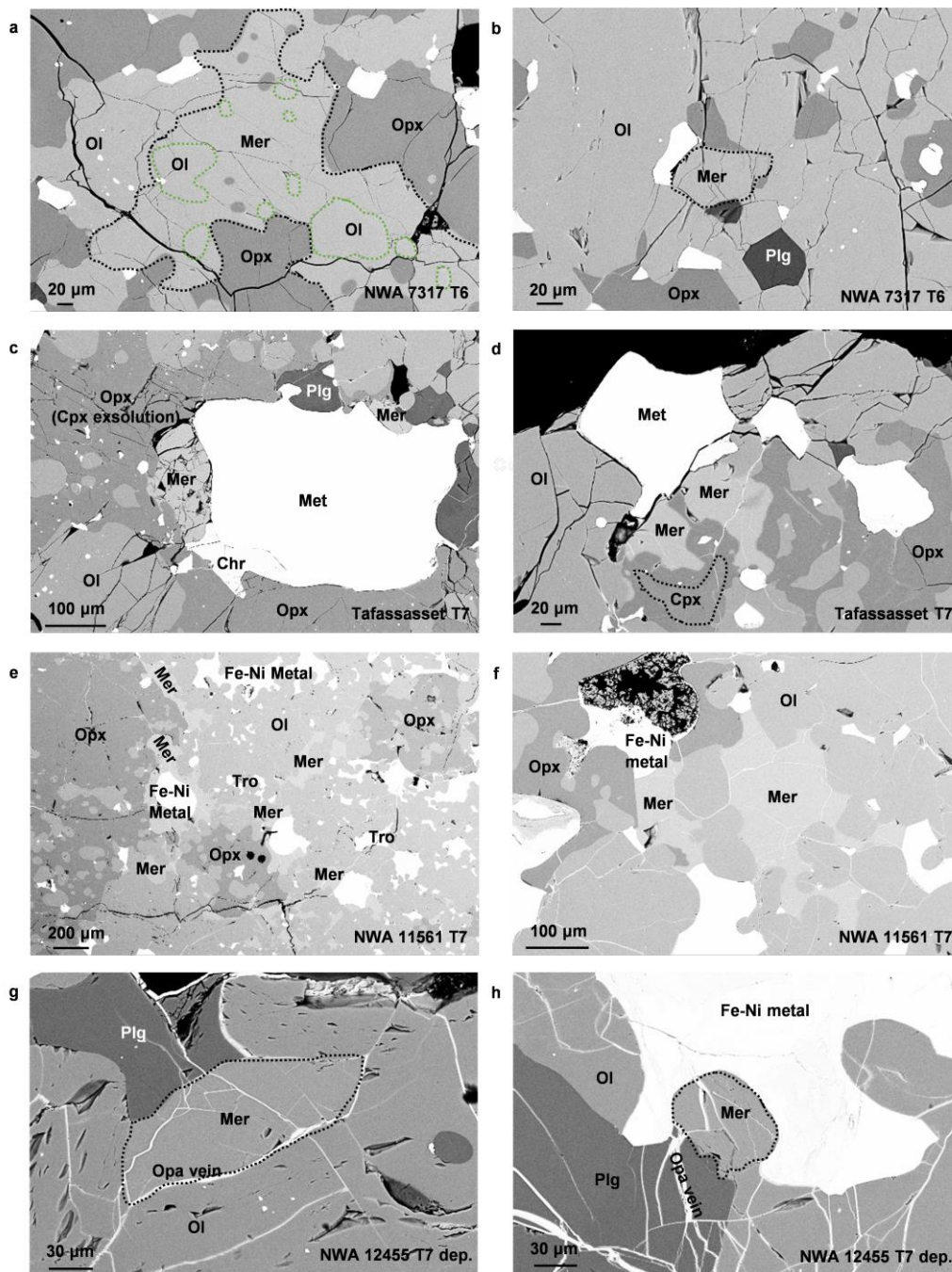


Figure S-7 Occurrence of merrillite in Tafassite meteorites. Coarsely grained merrillite (>100 μm) typically either as (a) oikocrysts with olivine (circled with green dotted lines) and pyroxene inclusions or (e) and (f) irregular and discontinuous patches. Finer sub-granular to irregular-shaped merrillites were commonly found in (c), (d) and (f) attached to opaque assemblages (Fe-Ni metal, troilite) or (b), (g) and (h) less commonly to other grain boundaries.

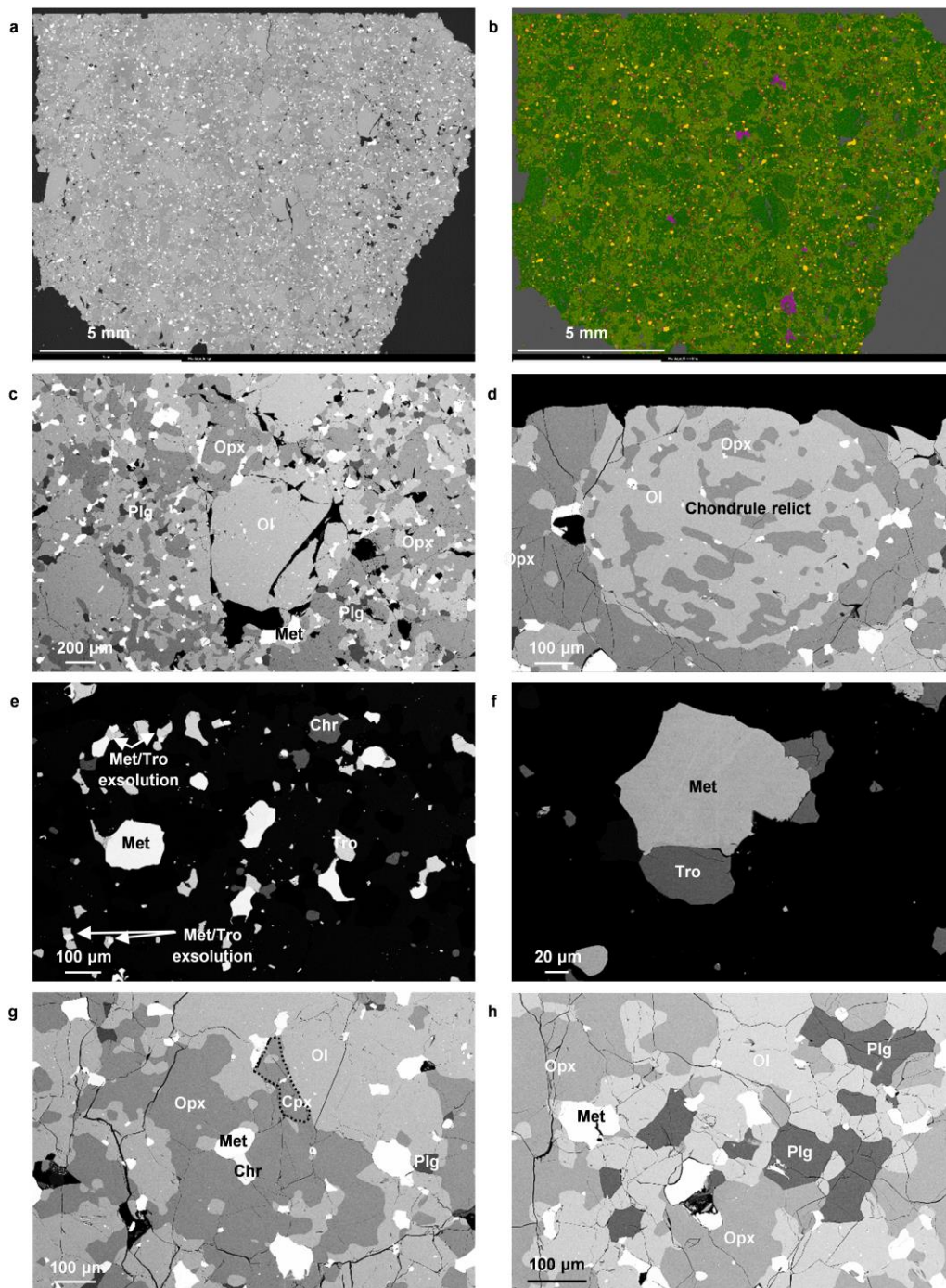


Figure S-8 Petrological observations of NWA 7317 T6 chondrite. **(a)** Multi-field BSE image. **(b)** Corresponding false-coloured phase map. **(c)** Poikiloblastic olivine set in recrystallised matrix. **(d)** Rare relict chondrule. **(e)** and **(f)** Opaques comprised of Fe-Ni metal, troilite (Tro, $T_{\text{peak}} > 1173$ K) and Al-rich chromite. **(g)** Both Ca-rich pyroxene and Ca-poor pyroxene are stable ($T_{\text{peak}} < 1353$ K). **(h)** Granular and homogeneous plagioclase with curved grain boundary, indicative of subsolidus heating ($T_{\text{peak}} < 1313$ K).

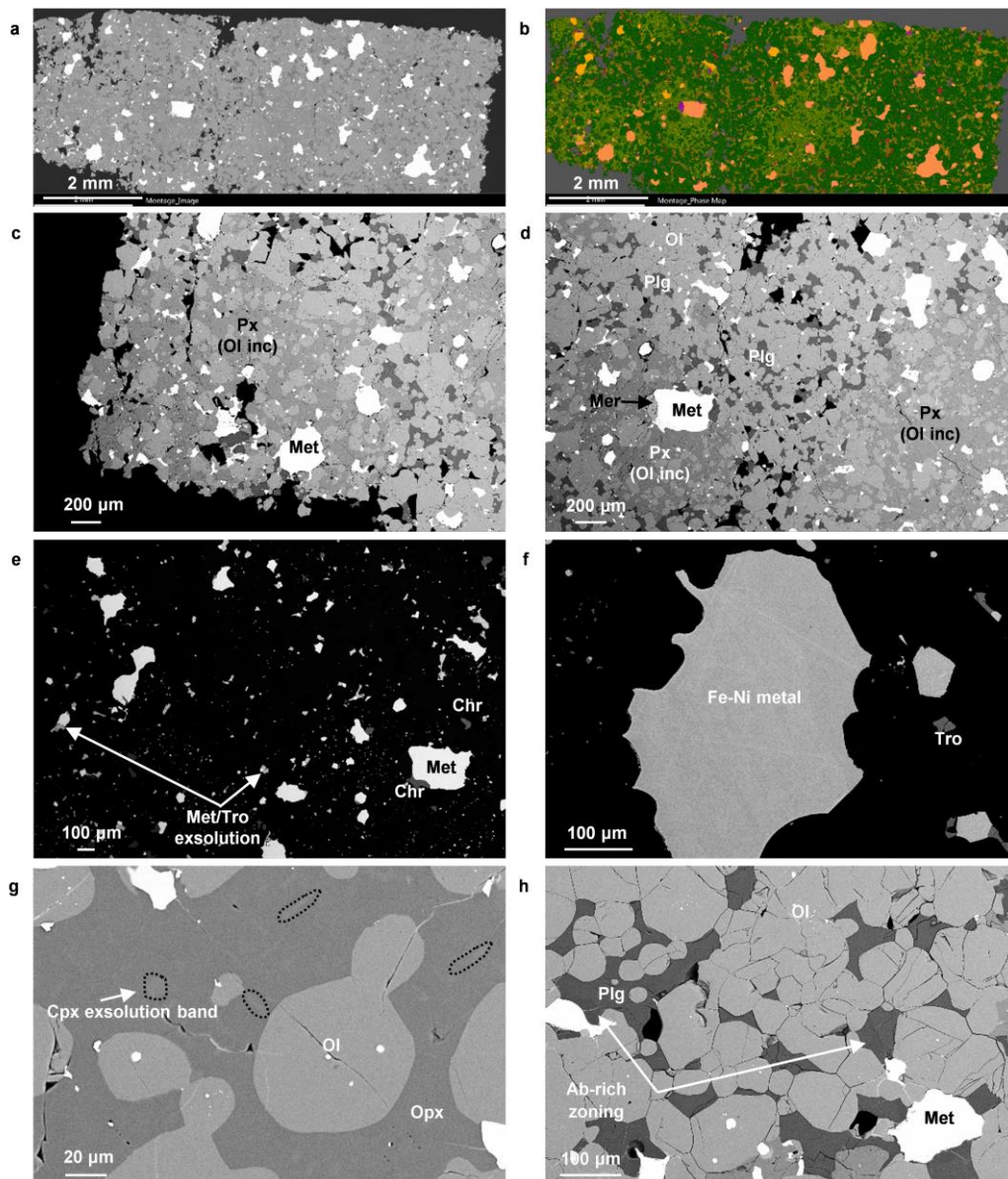


Figure S-9 Petrographic observations of Tafassasset T7 primitive achondrite. **(a)** Multi-field BSE images. **(b)** Corresponding false-coloured phase map. **(c-d)** Poikilitic pyroxene oikocrysts enclosing rounded olivine and opaques. **(e)** Opaques comprised of Fe-Ni metal, troilite (in exsolution texture, $T_{\text{peak}} > 1173$ K) and Al-rich chromite. **(f)** Fe-Ni metal; **(g)** Cpx exsolution lamellae (dotted lined) out of Opx (inverted pigeonite exsolution, $T_{\text{peak}} > 1353$ K). **(h)** Interstitial plagioclase with compositional heterogeneity as result of low degree of partial melting (supersolidus heating, $T_{\text{peak}} > 1313$ K).

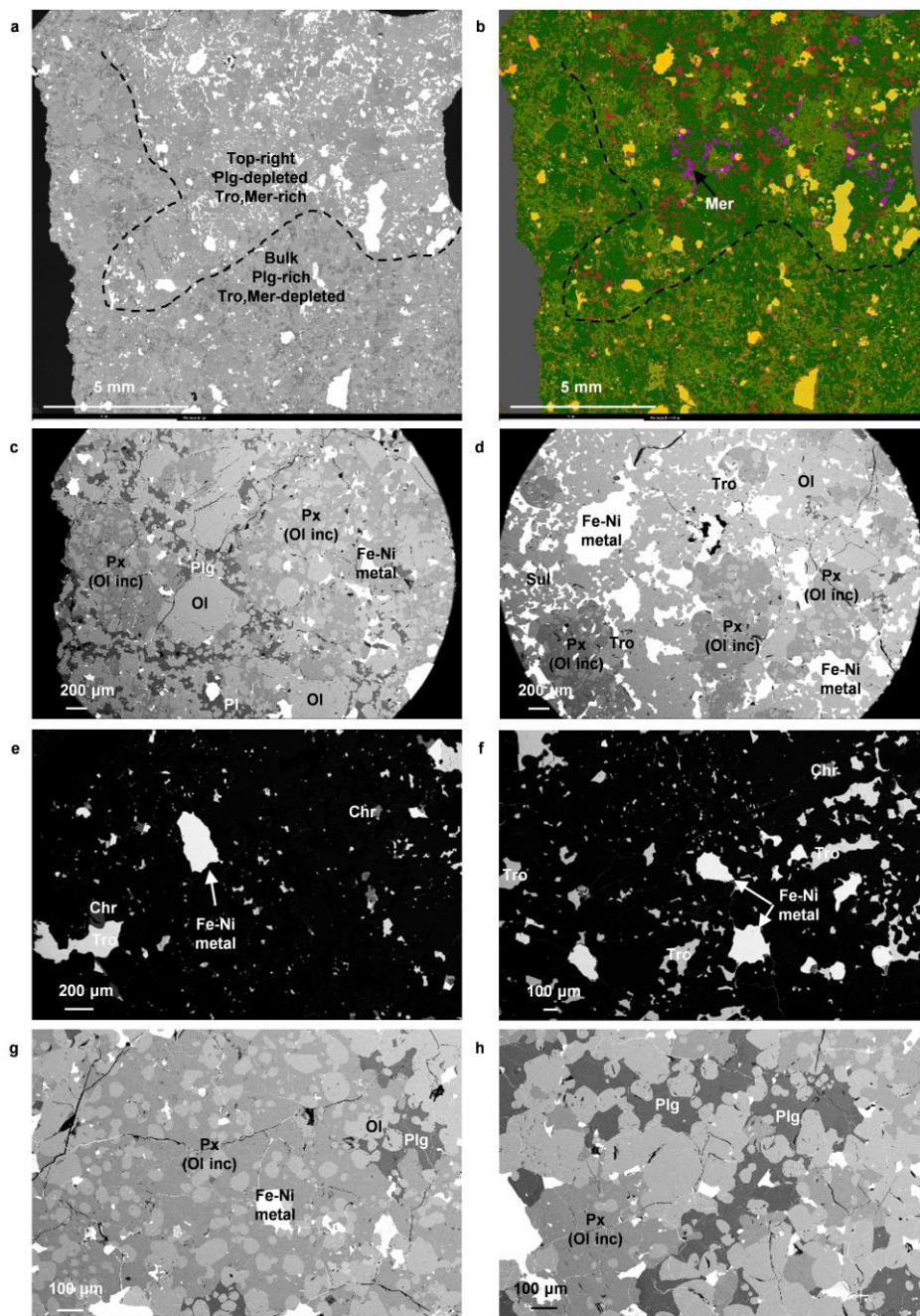


Figure S-10 Petrographic observations of NWA 11561 T7 primitive achondrite. **(a)** Multi-field BSE image. **(b)** Corresponding false-coloured phase map. **(c)** and **(d)** main Plg-rich, Tro, Mer-depleted lithology compared against Tro, Mer-rich, Plg-poor domain. **(e)** Opaques comprised of Fe-Ni metal, troilite (in exsolution texture, $T_{\text{peak}} > 1173$ K) and Al-rich chromite. and **(f)** Opaque-rich, Mer-rich Plg-depleted domain. Similar observations were also made on Tafassasset (Tomkins *et al.*, 2020). **(g)** Poikilitic pyroxenes. **(h)** Interstitial plagioclase with compositional heterogeneities due to partial melting ($T_{\text{peak}} > 1313$ K).

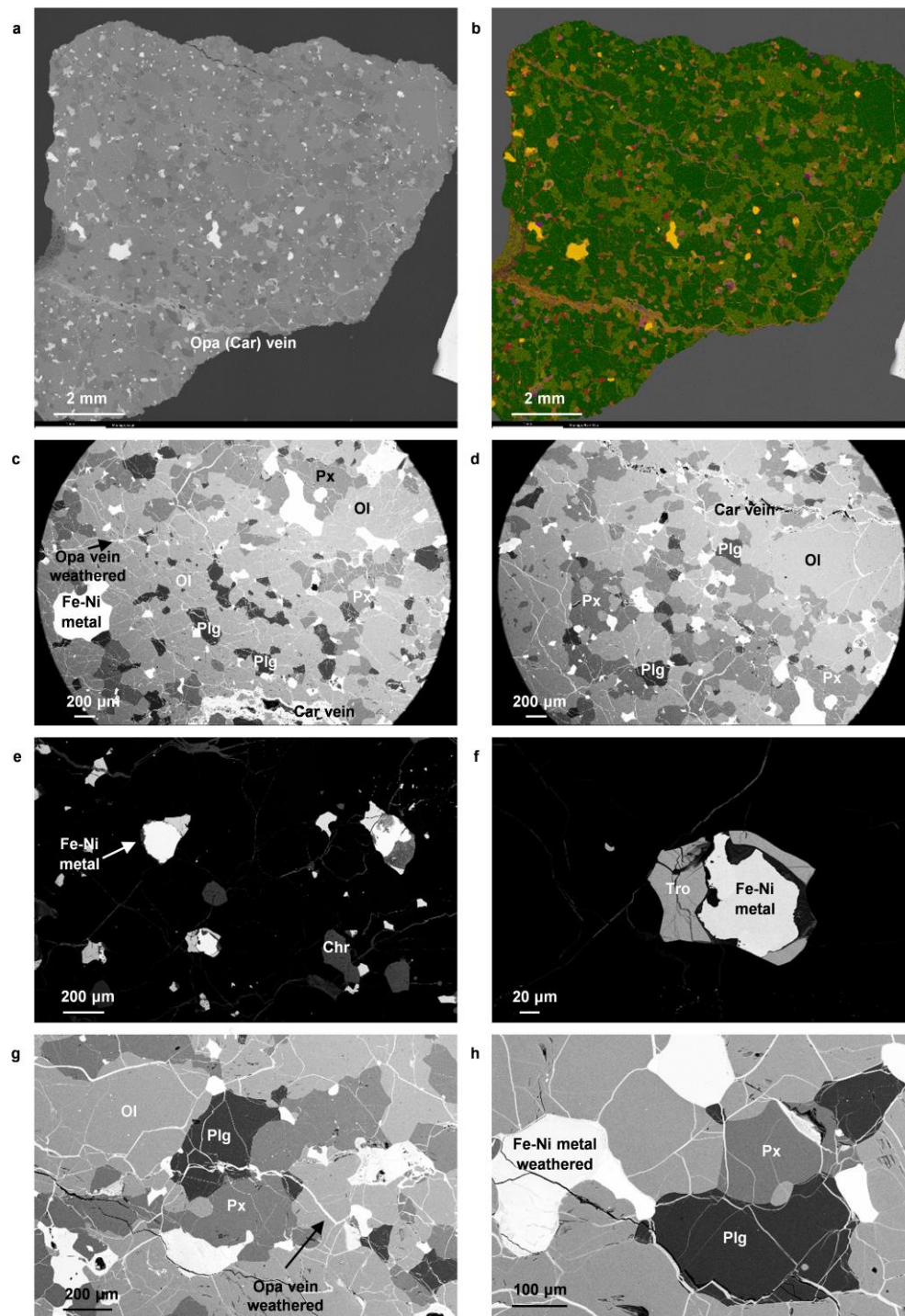


Figure S-11 Petrographic observations of NWA 12455 T7 depleted primitive achondrite. **(a)** Multi-field BSE image. **(b)** Corresponding false-coloured phase map. **(c)** and **(d)** Protogranular texture without chondrule relict. **(e-f)** Opaques. **(g)** Cpx and Opx exist as separate grains. **(h)** Granular and homogeneous plagioclase with curved grain boundary. This sample is depleted in incompatible components (Plg, Cpx, Mer), suggesting partial melt loss ($T_{\text{peak}} > 1313$ K).

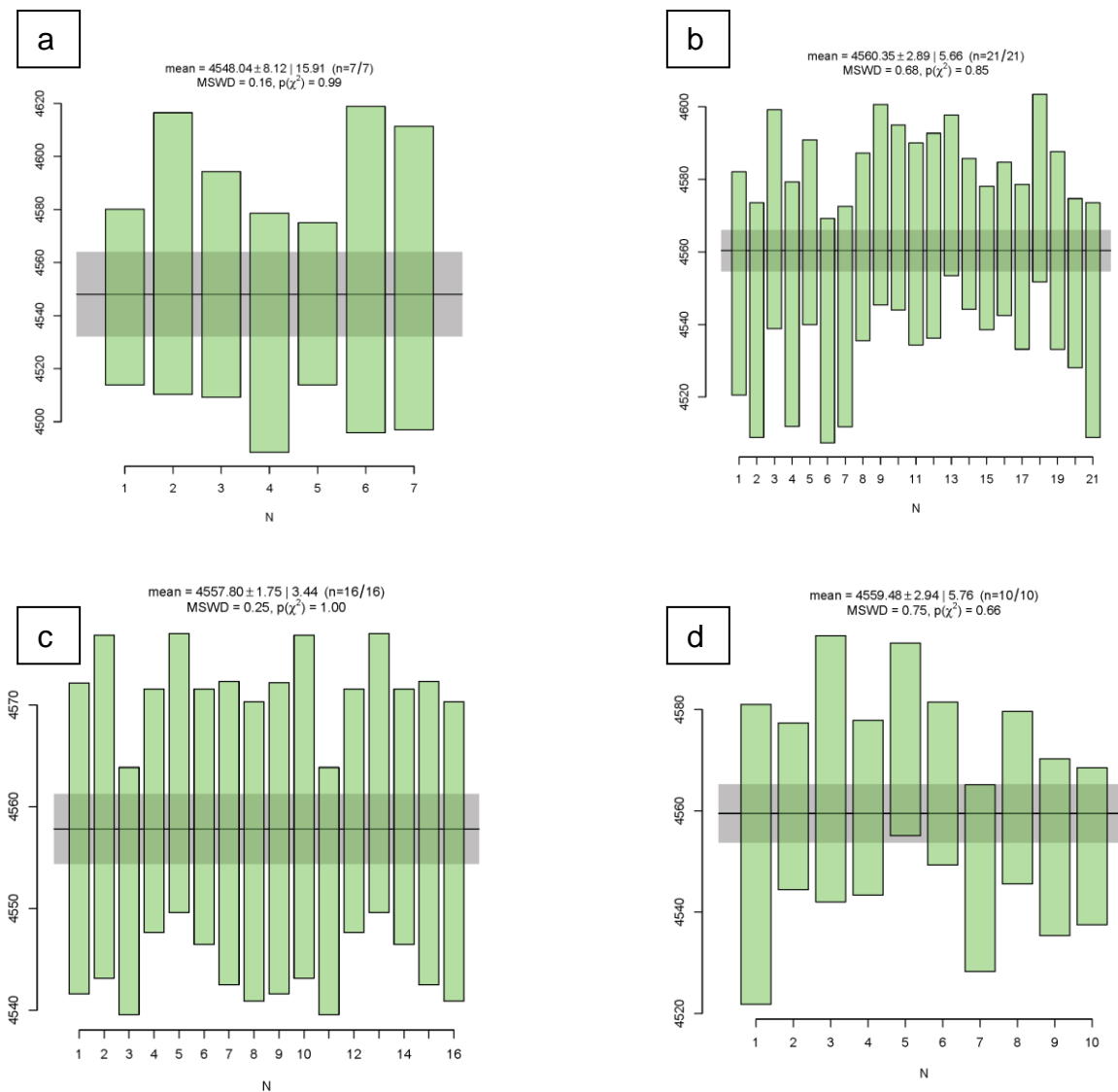


Figure S-12 SIMS Pb–Pb merrillite ages in Ma of Tafassite meteorites from this study: Tafassasset **(a)**, NWA 11561 **(b)**, NWA 12455 **(c)** and NWA 7317 **(d)**. Weighted averages of individual measurements (data in Table S-5) with respective 1σ and 95 % confidence interval uncertainties, number of analyses included, Mean Square of the Weighted Deviates (MSWD) and probability chi-squared p-value for the age homogeneity test. Number of analyses vary with number of suitable phosphates found in thin sections with different mineralogy and surface areas.

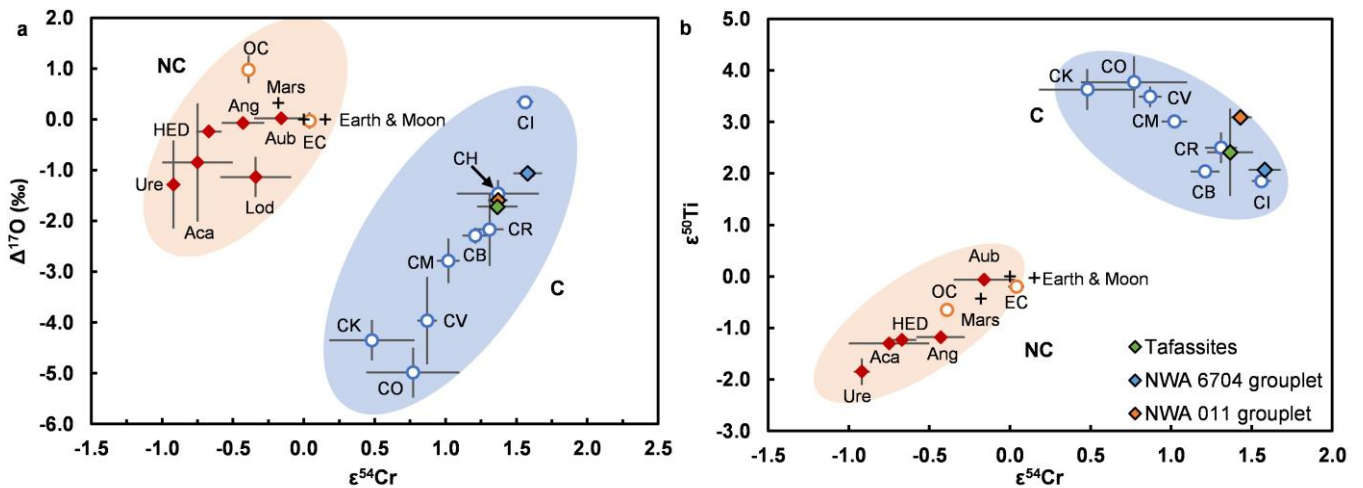


Figure S-13 NC-C isotopic dichotomy defined from bulk meteorite O, Cr and Ti isotopic anomalies. (a) Average compositions (2 s.d.) for $\epsilon^{54}\text{Cr}$ vs. $\Delta^{17}\text{O}$ and (b) $\epsilon^{54}\text{Cr}$ vs. $\epsilon^{50}\text{Ti}$ of Tafassites, NWA 011 and NWA 6704 grouplets (data in Table S-6) compared with other meteorite groups: acapulcoite (Aca), aubrite (Aub), angrite (Ang), brachinite (Bra), howardite-eucrite-diogenite (HED), lodranite (Lod), ureilite (Ure), carbonaceous chondrite groups (C), ordinary (OC) and enstatite chondrites (EC).

Supplementary Information References

- Agee, C. B., Aikin, H., Ziegler, K. (2020) Northwest Africa 12869: Primitive Achondrite from the CR2 Parent body or member of a new meteorite group? *51st Lunar and Planetary Science Conference*, 2292.
- Alexander, C.M.O.D., Howard, K.T., Bowden, R., Fogel, M.L. (2013) The classification of CM and CR chondrites using bulk H, C and N abundances and isotopic compositions. *Geochimica et Cosmochimica Acta* 123, 244–260. <https://doi.org/10.1016/j.gca.2013.05.019>
- Amelin, Y., Koefoed, P., Iizuka, T., Fernandes, V.A., Huyskens, M.H., Yin, Q.Z., Irving, A.J. (2019) U–Pb, Rb–Sr and Ar–Ar systematics of the ungrouped achondrites Northwest Africa 6704 and Northwest Africa 6693. *Geochimica et Cosmochimica Acta* 245, 628–642. <https://doi.org/10.1016/j.gca.2018.09.021>
- Andersen, D.J., Lindsley, D.H., Davidson, P.M. (1993) QUILF: A pascal program to assess equilibria among Fe–Mg–Mn–Ti oxides, pyroxenes, olivine, and quartz. *Computers & Geosciences* 19, 1333–1350. [https://doi.org/10.1016/0098-3004\(93\)90033-2](https://doi.org/10.1016/0098-3004(93)90033-2)
- Benedix, G.K., Lauretta, D.S., McCoy, T.J. (2005) Thermodynamic constraints on the formation conditions of winonaites and silicate-bearing IAB irons. *Geochimica et Cosmochimica Acta* 69, 5123–5131. <https://doi.org/10.1016/j.gca.2005.03.048>
- Bogdanovski, O., Lugmair, G.W. (2004) Manganese–Chromium Isotope Systematics of Basaltic Achondrite Northwest Africa 011. *35th Lunar and Planetary Science Conference*, 1715.
- Bollard, J., Kawasaki, N., Sakamoto, N., Olsen, M., Itoh, S., Larsen, K., Wielandt, D., Schiller, M., Connelly, J.N., Yurimoto, H., Bizzarro, M. (2019) Combined U-corrected Pb–Pb dating and ²⁶Al–²⁶Mg systematics of individual chondrules – Evidence for a reduced initial abundance of ²⁶Al amongst inner Solar System chondrules. *Geochimica et Cosmochimica Acta* 260, 62–83. <https://doi.org/10.1016/j.gca.2019.06.025>
- Bourot-Denise, M. (2002) Tafassasset: an equilibrated CR chondrite. *33rd Lunar and Planetary Science Conference*, 1611.
- Bouvier, A., Spivak-Birndorf, L.J., Brennecka, G.A., Wadhwa, M. (2011) New constraints on early Solar System chronology from Al–Mg and U–Pb isotope systematics in the unique basaltic achondrite Northwest Africa 2976. *Geochimica et Cosmochimica Acta* 75, 5310–5323. <https://doi.org/10.1016/j.gca.2011.06.033>
- Breton, T., Quitté, G., Toplis, M.J., Monnereau, M., Birck, J.L., Göpel, C., Charles, C. (2015) Tafassasset: Evidence of early incipient differentiation on a metal-rich chondritic parent body. *Earth and Planetary Science Letters* 425, 193–203. <https://doi.org/10.1016/j.epsl.2015.06.002>
- Burkhardt, C., Kleine, T., Oberli, F., Pack, A., Bourdon, B., Wieler, R. (2011) Molybdenum isotope anomalies in meteorites: Constraints on solar nebula evolution and origin of the Earth. *Earth and Planetary Science Letters* 312, 390–400. <https://doi.org/10.1016/j.epsl.2011.10.010>
- Burkhardt, C., Dauphas, N., Hans, U., Bourdon, B., Kleine, T. (2019) Elemental and isotopic variability in solar system materials by mixing and processing of primordial disk reservoirs. *Geochimica et Cosmochimica Acta* 261, 145–170. <https://doi.org/10.1016/j.gca.2019.07.003>
- Connolly, H.C., Zipfel, J., Folco, L., Smith, C., Jones, R.H., Benedix, G., Righter, K., Yamaguchi, A., Aoudjehane, H.C., Grossman, J.N. (2007a) The Meteoritical Bulletin, No. 91. *Meteoritics and Planetary Science* 42, 413–466. <https://doi.org/10.1111/j.1945-5100.2007.tb00242.x>
- Connolly, H.C., Smith, C., Benedix, G., Folco, L., Righter, K., Zipfel, J., Yamaguchi, A., Aoudjehane, C. (2007b) The Meteoritical Bulletin, No. 92. *Meteoritics and Planetary Science* 42, 1647–1694. <https://doi.org/10.1111/j.1945-5100.2007.tb00596.x>
- Dodd, R.T. (1969) Metamorphism of the ordinary chondrites: A review. *Geochimica et Cosmochimica Acta* 33. [https://doi.org/10.1016/0016-7037\(69\)90138-0](https://doi.org/10.1016/0016-7037(69)90138-0)
- Fischer-Gödde, M., Burkhardt, C., Kruijer, T.S., Kleine, T. (2015) Ru isotope heterogeneity in the solar protoplanetary disk. *Geochimica et Cosmochimica Acta* 168, 151–171. <https://doi.org/10.1016/j.gca.2015.07.032>
- Floss, C., Taylor, L.A., Promprated, P., Rumble, D. (2005) Northwest Africa 011: A ‘Euclitic’ basalt from a non-eucrite parent body. *Meteoritics and Planetary Science* 40, 343–360. <https://doi.org/10.1111/j.1945-5100.2005.tb00387.x>
- Gail, H.P., Trieloff, A. (2019) Thermal history modelling of the L chondrite parent body. *Astronomy and Astrophysics* 628, A77. <https://doi.org/10.1051/0004-6361/201936020>

- Gardner-Vandy, K.G., Lauretta, D.S., Greenwood, R.C., McCoy, T.J., Killgore, M., Franchi, I.A. (2012) The Tafassasset primitive achondrite: Insights into initial stages of planetary differentiation. *Geochimica et Cosmochimica Acta* 85, 142–159. <https://doi.org/10.1016/j.gca.2012.01.014>
- Garvie, L. (2012) The Meteoritical Bulletin, No. 99. *Meteoritics and Planetary Science* 47, 1–52.
- Gattacceca, J., McCubbin, F. M., Bouvier, A., Grossman, J.N. (2020) The Meteoritical Bulletin, No. 108. *Meteoritics and Planetary Science* 55, 1146–1150. <https://doi.org/10.1111/maps.13493>
- Ghiorso, M.S., Sack, R.O. (1991) An internally consistent model for the thermodynamic properties of Fe-Mg-oxides. *Contributions to Mineralogy and Petrology* 204, 474–505. <https://doi.org/10.1007/BF00321989>
- Ghiorso, M.S., Sack, R.O. (1995) Chemical mass transfer in magmatic processes IV. A revised and internally consistent thermodynamic model for the interpolation and extrapolation of liquid-solid equilibria in magmatic systems at elevated temperatures and pressures. *Contributions to Mineralogy and Petrology* 119, 197–212. <https://doi.org/10.1007/BF00307281>
- Göpel, C., Manhès, G., Allègre, C.J. (1994) U–Pb systematics of phosphates from equilibrated ordinary chondrites. *Earth and Planetary Science Letters* 121, 153–171. [https://doi.org/10.1016/0012-821X\(94\)90038-8](https://doi.org/10.1016/0012-821X(94)90038-8)
- Göpel, C., Birck, J.L., Galy, A., Barrat, J.A., Zanda, B. (2015) Mn–Cr systematics in primitive meteorites: Insights from mineral separation and partial dissolution. *Geochimica et Cosmochimica Acta* 156, 1–24. <https://doi.org/10.1016/j.gca.2015.02.008>
- Henke, S., Gail, H.P., Trielloff, M., Schwarz, W.H., Kleine, T. (2012) Thermal history modelling of the H chondrite parent body. *Astronomy and Astrophysics* 545, 1–21. <https://doi.org/10.1051/0004-6361/201219100>
- Hiess, J., Condon, D.J., McLean, N., Noble, S.R. (2012). $^{238}\text{U}/^{235}\text{U}$ systematics in terrestrial uranium-bearing minerals. *Science* 335, 1610–1614. <https://doi.org/10.1126/science.1215507>
- Hibiya, Y., Archer, G.J., Tanaka, R., Sanborn, M.E., Sato, Y., Iizuka, T., Ozawa, K., Walker, R.J., Yamaguchi, A., Yin, Q.Z., Nakamura, T., Irving, A.J. (2019) The origin of the unique achondrite Northwest Africa 6704: Constraints from petrology, chemistry and Re–Os, O and Ti isotope systematics. *Geochimica et Cosmochimica Acta* 245, 597–627. <https://doi.org/10.1016/j.gca.2018.04.031>
- Irving, A.J., Kuehner, S.M., Tanaka, R., Rumble, D., Ziegler, K., Sanborn, M.E., Yin, Q. (2014) Collisional disruption of a layered, differentiated CR parent body containing metamorphic and igneous lithologies overlain by a chondrite veneer. *45th Lunar and Planetary Science Conference*, 2465.
- Ito, M., Ganguly, J. (2006) Diffusion kinetics of Cr in olivine and ^{53}Mn – ^{53}Cr thermochronology of early solar system objects. *Geochimica et Cosmochimica Acta* 70, 799–809. <https://doi.org/10.1016/j.gca.2005.09.020>
- Kretz, R. (1982) Transfer and exchange equilibria in a portion of the pyroxene quadrilateral as deduced from natural and experimental data. *Geochimica et Cosmochimica Acta* 46, 411–421. [https://doi.org/10.1016/0016-7037\(82\)90232-0](https://doi.org/10.1016/0016-7037(82)90232-0)
- Koefoed, P. (2017) Sequencing planetary accretion using chronology of ungrouped achondrite. Australian National University, Thesis (PhD), <https://doi.org/10.25911/5d6c3eed488f1>
- Larimer, J.W. (1968) Experimental studies on the system Fe-MgO-SiO₂-O₂ and their bearing on the petrology of chondritic meteorites. *Geochimica et Cosmochimica Acta* 32, 1187–1207. [https://doi.org/10.1016/0016-7037\(68\)90121-X](https://doi.org/10.1016/0016-7037(68)90121-X)
- Lindsley, D.H., Andersen, D.J. (1983) A two-pyroxene thermometer. *Journal of Geophysical Research* 88, A887. <https://doi.org/10.1029/JB088iS02p0A887>
- Miller, M.F. (2002) Isotopic fractionation and the quantification of ^{17}O anomalies in the oxygen three-isotope system: an appraisal and geochemical significance. *Geochimica et Cosmochimica Acta* 66, 1881–1889. [https://doi.org/10.1016/S0016-7037\(02\)00832-3](https://doi.org/10.1016/S0016-7037(02)00832-3)
- Neumann, W., Breuer, D., Spohn, T. (2012) Differentiation and core formation in accreting planetesimals. *Astronomy and Astrophysics* 543. <https://doi.org/10.1051/0004-6361/201219157>
- Neumann, W., Breuer, D., Spohn, T. (2014) Modelling of compaction in planetesimals. *Astronomy and Astrophysics* 567, 1–15. <https://doi.org/10.1051/0004-6361/201423648>
- Neumann, W., Henke, S., Breuer, D., Gail, H.P., Schwarz, W.H., Trielloff, M., Hopp, J., Spohn, T. (2018) Modeling the evolution of the parent body of acapulcoites and lodranites: A case study for partially differentiated asteroids. *Icarus* 311, 146–169. <https://doi.org/10.1016/j.icarus.2018.03.024>

- O'Neill, H.S.C., Pownceby, M.I. (1993) Thermodynamic data from redox reactions at high temperatures. I. An experimental and theoretical assessment of the electrochemical method using stabilized zirconia electrolytes, with revised values for the Fe-"FeO", Co-CoO, Ni-NiO and Cu-Cu₂O oxygen buffer. *Contributions to Mineralogy and Petrology* 114, 296–314. <https://doi.org/10.1007/BF01046533>
- Pape, J., Mezger, K., Bouvier, A.S., Baumgartner, L.P. (2019) Time and duration of chondrule formation: Constraints from ²⁶Al-²⁶Mg ages of individual chondrules. *Geochimica et Cosmochimica Acta* 244, 416–436. <https://doi.org/10.1016/j.gca.2018.10.017>
- Papike, J.J., Karner, J.M., Shearer, C.K. (2003) Determination of planetary basalt parentage: A simple technique using the electron microprobe. *American Mineralogist* 88, 469–472. <https://doi.org/10.2138/am-2003-2-323>
- Righter, K., Neff, K.E. (2007) Temperature and oxygen fugacity constraints on CK and R chondrites and implications for water and oxidation in the early solar system. *Polar Science* 1, 25–44. <https://doi.org/10.1016/j.polar.2007.04.002>
- Righter, K., Drake, M.J., Scott, E.R.D. (2006) Compositional relationships between meteorites and terrestrial planets. *Meteorites and the early solar system II* 943, 803–828. <https://doi.org/10.2307/j.ctv1v7zdm4.43>
- Russell, S.S., Zipfel, J., Grossman, J.N., Grady, M.M. (2002) The Meteoritical Bulletin, No. 86. *Meteoritics and Planetary Science* 37, A157–A184. <https://doi.org/10.1111/j.1945-5100.2002.tb00913.x>
- Russell, S.S., Zolensky, M., Righter, K., Folco, L., Jones, R., Connolly, H.C., Grady, M.M., Grossman, J.N. (2005) The Meteoritical Bulletin, No. 89. *Meteoritics and Planetary Science* 40, A201–A263. <https://doi.org/10.1111/j.1945-5100.2005.tb00425.x>
- Ruzicka, A., Grossman, J., Bouvier, A., Agee, C.B. (2013) The Meteoritical Bulletin, No. 103. *Meteoritics & Planetary Science* 52, 1–244.
- Ruzicka, A., Grossman, J.N., Garvie, L. (2014) The Meteoritical Bulletin, No. 100. *Meteoritics and Planetary Science* 49, 1–101. <https://doi.org/10.1111/maps.12342>
- Ruzicka, A., Grossman, J., Bouvier, A., Herd, C.D.K., Agee, C.B. (2015) The Meteoritical Bulletin, No. 101. *Meteoritics and Planetary Science* 50, 1661–1661. <https://doi.org/10.1111/maps.12490>
- Sack, R.O., Ghiorso, M.S. (1989) Importance of considerations of mixing properties in establishing an internally consistent thermodynamic database: thermochemistry of minerals in the system Mg₂SiO₄-Fe₂SiO₄-SiO₂. *Contributions to Mineralogy and Petrology* 102, 41–68. <https://doi.org/10.1007/BF01160190>
- Sack, R.O., Ghiorso, M.S. (1991) Chromian spinels as petrogenetic indicators: thermodynamics and petrological applications. *American Mineralogist* 76, 827–847.
- Sack, R.O., Ghiorso, M.S. (1994a) Thermodynamics of multicomponent pyroxenes: I. Formulation of a general model. *Contributions to Mineralogy and Petrology* 116, 277–286. <https://doi.org/10.1007/BF00306497>
- Sack, R.O., Ghiorso, M.S. (1994b) Thermodynamics of multicomponent pyroxenes: II. Phase relations in the quadrilateral. *Contributions to Mineralogy and Petrology* 116, 287–300. <https://doi.org/10.1007/BF00306498>
- Sack, R.O., Ghiorso, M.S. (1994c) Thermodynamics of multicomponent pyroxenes: III. Calibration of Fe²⁺(Mg)₋₁, TiAl₂(MgSi₂)₋₁, TiFe³⁺₂(MgSi₂)₋₁, AlFe³⁺(MgSi)₋₁, NaAl(CaMg)₋₁, Al₂(MgSi)₋₁ and Ca(Mg)₋₁ exchange reactions between pyroxenes and silicate melts. *Contributions to Mineralogy and Petrology* 118, 271–296. <https://doi.org/10.1007/BF00306648>
- Sanborn, M.E., Wimpenny, J., Williams, C.D., Yamakawa, A., Amelin, Y., Irving, A.J., Yin, Q.Z. (2019) Carbonaceous achondrites Northwest Africa 6704/6693: Milestones for early Solar System chronology and genealogy. *Geochimica et Cosmochimica Acta* 245, 577–596. <https://doi.org/10.1016/j.gca.2018.10.004>
- Schrader, D.L., McCoy, T.J., Gardner-Vandy, K.G. (2017a) Relict chondrules in primitive achondrites: Remnants from their precursor parent bodies. *Geochimica et Cosmochimica Acta* 205, 295–312. <https://doi.org/10.1016/j.gca.2017.02.012>
- Schrader, D.L., Nagashima, K., Krot, A.N., Oglione, R.C., Yin, Q.Z., Amelin, Y., Stirling, C.H., Kaltenbach, A. (2017b) Distribution of ²⁶Al in the CR chondrite chondrule-forming region of the protoplanetary disk. *Geochimica et Cosmochimica Acta* 201, 275–302. <https://doi.org/10.1016/j.gca.2009.12.016>
- Schulz, T., Münker, C., Mezger, K., Palme, H. (2010) Hf–W chronometry of primitive achondrites. *Geochimica et Cosmochimica Acta* 74, 1706–1718. <https://doi.org/10.1016/j.gca.2009.12.016>
- Schwenn, M.B., Goetze, C. (1978) Creep of olivine during hot-pressing. *Tectonophysics* 48, 41–60. <https://doi.org/10.1016/0040->

[1951\(78\)90085-9](#)

- Stacey, J.S., Kramers, J.D. (1975) Approximation of terrestrial lead isotope evolution by a two-stage model. *Earth and Planetary Science Letters* 26, 207–221. [https://doi.org/10.1016/0012-821X\(75\)90088-6](https://doi.org/10.1016/0012-821X(75)90088-6)
- Steiger, R.H., Jäger, E. (1977) Subcommission on geochronology: Convention on the use of decay constants in geo- and cosmochronology. *Earth and Planetary Science Letters* 36, 359–362. [https://doi.org/10.1016/0012-821X\(77\)90060-7](https://doi.org/10.1016/0012-821X(77)90060-7)
- Sugiura, N., Yamaguchi, A. (2007) Al–Mg and Mn–Cr ages of Northwest Africa 011 achondrite. 38th *Lunar and Planetary Science Conference*, 1431.
- Sugiura, N., Fujiya, W. (2014) Correlated accretion ages and $\epsilon^{54}\text{Cr}$ of meteorite parent bodies and the evolution of the solar nebula. *Meteoritics and Planetary Science* 49, 772–787. <https://doi.org/10.1111/maps.12292>
- Tatsumoto, M., Knight, R.J., Allegre, C.J. (1973) Time differences in the formation of meteorites as determined from the ratio of lead-207 to lead-206. *Science* 180, 1279–1283. <https://doi.org/10.1126/science.180.4092.1279>
- Thomson, S.N., Gehrels, G.E., Ruiz, J., Buchwaldt, R. (2012) Routine low-damage apatite U–Pb dating using laser ablation-multicollector- ICPMS. *Geochemistry, Geophysics, Geosystems* 13, 1–23. <https://doi.org/10.1029/2011GC003928>
- Tomkins, A.G., Johnson, T.E., Mitchell, J.T. (2020) A review of the chondrite–achondrite transition, and a metamorphic facies series for equilibrated primitive stony meteorites. *Meteoritics and Planetary Science* 55, 857–885. <https://doi.org/10.1111/maps.13472>
- Trinquier, A., Elliott, T., Ulfbeck, D., Coath, C., Krot, A.N., Bizzarro, M. (2009) Origin of nucleosynthetic isotope heterogeneity in the solar protoplanetary disk. *Science* 324, 374–376. <https://doi.org/10.1126/science.1168221>
- Van Kooten, E.M.M.E., Wielandt, D., Schiller, M., Nagashima, K., Thomen, A., Larsen, K.K., Olsen, M.B., Nordlund, Å., Krot, A.N., Bizzarro, M. (2016) Isotopic evidence for primordial molecular cloud material in metal-rich carbonaceous chondrites. *Proceedings of the National Academy of Sciences* 113, 2011–2016. <https://doi.org/10.1073/pnas.1518183113>
- Warren, P.H., Rubin, A.E., Isa, J., Brittenham, S., Ahn, I., Choi, B.G. (2013) Northwest Africa 6693: A new type of FeO-rich, low- $\Delta 17\text{O}$, poikilitic cumulate achondrite. *Geochimica et Cosmochimica Acta* 107, 135–154. <https://doi.org/10.1016/j.gca.2012.12.025>
- Weisberg, M.K., McCoy, T.J., Krot, A.N. (2006) Systematics and Evaluation of Meteorite Classification. In: Lauretta, D.S., McSween, H.Y. (Eds.) *Meteorites and the early solar system II*, 19–52. <https://doi.org/10.2307/j.ctv1v7zdm8>
- Weisberg, M.K., Smith, C., Benedix, G., Herd, C.D.K., Righter, K., Haack, H., Yamaguchi, A., Chennaoui Aoudjehane, H., Grossman, J.N. (2010) The Meteoritical Bulletin, No. 97. *Meteoritics and Planetary Science* 45, 449–493. <https://doi.org/10.1111/j.1945-5100.2010.01036.x>
- Yamaguchi, A., Clayton, R.N., Mayeda, T.K., Ebihara, M., Oura, Y., Miura, Y.N., Haramura, H., Misawa, K., Kojima, H., Nagao, K. (2002) A new source of basaltic meteorites inferred from Northwest Africa 011. *Science* 296, 334–336. <https://doi.org/10.1126/science.1069408>

